



HAL
open science

Giant Diffusion of Nanomechanical Rotors in a Tilted Washboard Potential

Louis Bellando, Melissa Kleine, Yacine Amarouchene, Mathias Perrin, Yann Louyer

► **To cite this version:**

Louis Bellando, Melissa Kleine, Yacine Amarouchene, Mathias Perrin, Yann Louyer. Giant Diffusion of Nanomechanical Rotors in a Tilted Washboard Potential. *Physical Review Letters*, 2022, 129 (023602), 10.1103/PhysRevLett.129.023602 . hal-03633285v2

HAL Id: hal-03633285

<https://hal.science/hal-03633285v2>

Submitted on 12 Jul 2022

HAL is a multi-disciplinary open access archive for the deposit and dissemination of scientific research documents, whether they are published or not. The documents may come from teaching and research institutions in France or abroad, or from public or private research centers.


L'archive ouverte pluridisciplinaire **HAL**, est destinée au dépôt et à la diffusion de documents scientifiques de niveau recherche, publiés ou non, émanant des établissements d'enseignement et de recherche français ou étrangers, des laboratoires publics ou privés.



Distributed under a Creative Commons Attribution 4.0 International License

Giant Diffusion of Nanomechanical Rotors in a Tilted Washboard Potential

L. Bellando,^{*} M. Kleine,[Ⓛ] Y. Amarouchene,^{Ⓛ,†} M. Perrin,^{Ⓛ,‡} and Y. Louyer[§]
Université de Bordeaux, CNRS, LOMA, UMR 5798, F-33405 Talence, France

 (Received 5 April 2022; accepted 15 June 2022; published 6 July 2022)

We present an experimental realization of a biased optical periodic potential in the low friction limit. The noise-induced bistability between locked (torsional) and running (spinning) states in the rotational motion of a nanodumbbell is driven by an elliptically polarized light beam tilting the angular potential. By varying the gas pressure around the point of maximum intermittency, the rotational effective diffusion coefficient increases by more than 3 orders of magnitude over free-space diffusion. These experimental results are in agreement with a simple two-state model that is derived from the Langevin equation through using timescale separation. Our work provides a new experimental platform to study the weak thermal noise limit for diffusion in this system.

DOI: [10.1103/PhysRevLett.129.023602](https://doi.org/10.1103/PhysRevLett.129.023602)

Thermal diffusion in a tilted periodic (also named washboard) potential constitutes an archetypal model of transport phenomena in nonequilibrium statistical physics [1,2]. It describes a diverse range of systems, including Josephson junctions [3], molecular motors [4], synchronization phenomena [5], and diffusion on crystal surfaces [6], to name only a few.

Brownian particles moving in the tilted potential at nonzero temperature exhibit two distinct well-characterized limiting behaviors: locked and running states. The first emerges when the potential wells are deeper than the thermal energy scale, the diffusing particle remains in a local minimum. In the latter, a sufficient tilt of the potential, lowering its energy barrier, allows the particle to flow down the potential wells. Depending on the system parameters (friction, temperature, and tilt), both solutions may coexist, and stochastic transitions between locked and running states may occur. It has been shown, both experimentally [4,7,8] and theoretically [9,10], that in this two-state coexistence regime, the effective diffusion coefficient can be enhanced by several orders of magnitude relative to the free diffusion coefficient. However, this has only been experimentally observed in the overdamped regime which is by now a fully understood stochastic process [2].

To our knowledge, an experimental study of giant diffusion in the strongly inertial (underdamped) regime is still missing. The theoretical problem is also more demanding in the underdamped and weak noise limits because the usual expansion of the matrix continued fraction [2] fails to converge well [11]. On these grounds, this nonlinear stochastic system in the low-noise and low-damping limits is still attractive [11].

We propose a simple experimental setup based on the optical trapping of a nanodumbbell in a moderate vacuum. A special feature of our experiment is that the friction coefficient, being linearly proportional to the gas pressure

P , can be tuned over several orders of magnitude. Therefore, for a nearly constant temperature, Brownian motion can move from the overdamped to the underdamped regime. This makes the optical trapping setup a suitable platform to study stochastic dynamics in the low-friction regime [12–14].

The main focus of this Letter is the analysis of the rotational diffusivity in the bistability region for an underdamped stochastic mechanical nanorotor traveling in a tilted periodic potential. We provide experimental confirmation of a giant diffusivity by tracking the rotational motion of a single silica nanodimer. Because of the experimentally achieved timescale separation, we show that the effective diffusion is well described by a two-state model for this nearly one-dimensional rotational motion.

The experimental setup consists of a vacuum optical tweezer trapping a dielectric silica dumbbell made of two nanospheres of nominal radius 68 ± 7 nm [15,16]. The continuous wave trapping laser beam (wavelength, $\lambda = 1064$ nm and power, 180 mW) passes through an objective lens with a 0.8 numerical aperture, the polarization's ellipticity of which can be changed by a quarter-wave plate. A detailed description of the experimental setup, calibration, and processing procedures is given in the Supplemental Material [17] including Refs. [18–32]. The shape and the size of the dimer are assessed under linear polarization, and correspond to an aspect ratio $L/D = 1.8$, with two spheres of radius $R_p = 65.7$ nm, where $D = 2R_p$ and L is the major axis length of the dimer. Our detection system is able to simultaneously record the particle's center of mass motion and its angular displacement.

The nanodimer experiences both a trapping force and a torque, both of which are induced by elliptically polarized light. In particular, when such an asymmetric Rayleigh scatterer lies in the transverse (\hat{x}, \hat{y}) plane, corresponding to $\theta = \pi/2$, the torque reads

$$M = M_C - M_L \sin(2\varphi), \quad (1)$$

where φ is the angle between the dimer main axis and the lab's horizontal \hat{x} axis. Its time evolution is related to the dimer rotation around the \hat{z} optical axis. M_C and M_L are respectively the *circular* and *linear* contributions of the optical torque which depend on the dimer polarizability tensor and the laser beam polarization [17].

In a linearly polarized optical tweezer, where $M_C = 0$, the long axis of the dimer (i.e., in the direction of greatest polarizability) will tend to align with the laser beam polarization. This is because the polarizability of the dimer along its long axis is greater than the polarizability perpendicular to it. As a result, the dimer acts as a torsion balance with a linear restoring torque, $-2M_L\varphi$. The libration pulsation Ω_L is well approximated in the low friction limit ($\Gamma_\varphi \ll \Omega_L$) by $\sqrt{2M_L/I_\perp}$, where I_\perp is the moment of inertia.

In contrast, for a circularly polarized trap, where $M_L = 0$, the asymmetric particle undergoes a constant torque, whatever its orientation φ . As a result of the continuous transfer of angular momentum, the particle will spin about the \hat{z} axis at constant frequency, as given by $\Omega_R = M_C/I_\perp\Gamma_\varphi$, where Γ_φ is the rotation or torsional vibration damping rate about the \hat{z} optical axis (see Ref. [17] for its determination). Note that the rotation frequency can exceed GHz, which allows us to study material stresses due to centrifugal forces [33,34], measure ultraweak torques [35,36], and examine quantum features of rotation [37,38].

Figure 1(a) illustrates the potential landscape and orientational dynamics for different polarization states. Considering the general case, for elliptical polarization, the potential has a washboard shape: $U(\varphi) = M_L \sin^2(\varphi) - M_C\varphi$, and one can observe running and locked states. Below, we only consider elliptical polarization which is held constant at $\phi_{\lambda/4} = 25^\circ$, the angle of the quarter-wave plate.

The dynamics of an asymmetric Brownian particle trapped under elliptically polarized light is six dimensional with translational and rotational degrees of freedom coupled to each other. This generally leads to a highly nonlinear problem [36,39,40]. However, in the following, we show that the giant diffusion phenomenon is well described by one-dimensional rotational dynamics. Comparison between the experiment and numerical simulations is made quantitative provided that an additional term is added to the usual *extinction* optical torque ($\propto \Re[\mathbf{p} \times \mathbf{E}_{\text{inj}}]$, with \mathbf{p} the dipole moment and \mathbf{E}_{inj} the incident electric field). This extra term, called *scattering* torque ($\propto \Im[\mathbf{p} \times \mathbf{p}^*]$), is due to the interference of the fields scattered by the particle [17,41]. This φ angle dynamics reproducing the stochastic jumps between torsion and continuous rotation states is described by the Langevin equation

$$I_\perp \ddot{\varphi} = -I_\perp \Gamma_\varphi \dot{\varphi} + M + M_{\text{th}}, \quad (2)$$

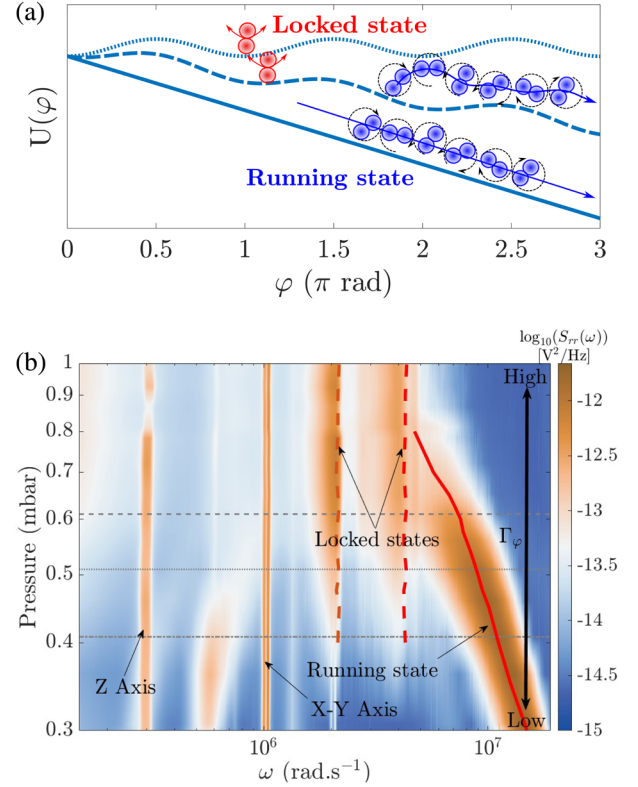


FIG. 1. (a) Illustration of the energy landscape for the rotation of the Brownian dimer around the optical axis for three different tilts. When the polarization is linear (blue dotted line), the potential is not tilted and the orientation of the dimer remains in the locked state. Conversely, for a circular polarization (solid blue line) the potential wells disappear. For elliptical polarization (dashed line), the rotational motion can change from a running state (spinning) to a locked state (torsional) and vice versa. (b) Surface plot in log-log scales of the angular vibration and translational power spectral densities as a function of the gas pressure for a beam ellipticity of $\phi_{\lambda/4} = 25^\circ$ and an optical power of 180 mW. The solid and dashed curves (red) represent the local maxima of the PSD computed by Langevin simulations of Eq. (2). The three grey horizontal curves at 0.41 mbar, 0.51 mbar, and 0.61 mbar outline the two-state coexistence region where the middle line denotes the maximum of intermittency.

where Γ_φ is the rotational damping rate and $M_{\text{th}} = \sqrt{2k_B T I_\perp \Gamma_\varphi} \zeta(t)$ is the thermal torque with $\zeta(t)$ a Gaussian noise of zero mean value. M is given by Eq. (1).

Figure 1(b) shows the position and orientation power spectral densities as a function of pressure, along with the numerical Langevin simulations (solid red curves). For consistency, we also show the frequencies associated with translational motions in the X , Y , and Z directions that are independent of gas pressure. The observed nondegeneracy of the transverse frequencies X , Y is expected for a noncircularly polarized laser beam. In the high friction limit, the torsional dynamics dominate the dimer orientation motion and their resonance frequencies remain constant in relation to pressure. Conversely, the rotational

dynamics is dominant in the low friction regime, i.e., at low pressure, and its angular frequency, Ω_R , rises as the inverse of the gas damping.

The red solid curves in Fig. 1(b) show a good agreement between the experiment and one-dimensional simulations of Eq. (2). One can also clearly see that the bistability region is quantitatively well described by the model. The two locked states observed in the spectral densities are also found in the numerical simulations, and correspond to the fundamental peak and its overtone. Although not within the scope of this Letter, we do not preclude contributions with other angles leading to coupling with extra motional degrees of freedom. The experimental determination of the dimer size and shape by the calibration procedure [17] is used for calculating the moments of inertia and polarizabilities. The latter are further supported numerically using COMSOL MULTIPHYSICS. We find that $I_{\perp} = 2 \times 10^{-32}$ kg m², M_C and M_L are, respectively, of the order of 2×10^{-22} N m and 6×10^{-20} N m, in good agreement with both experimental and numerical results.

As mentioned above, in the calculation of optical torques the contribution of *scattering* is included in addition to the usual *extinction* contribution [41]. Since the polarization of the trapping beam is not linear, this scattering torque is crucial to reproduce quantitatively the experimental results, particularly when the dimer spins. In many previous works, the scattering torque was ignored because the rotational Langevin equation was only qualitatively discussed. It is worth noting that if the scattering torque is not taken into account, the particle's rotation speed is overestimated by typically an order of magnitude for the actual dimer [17] and much more for a spheroid (data not shown). Some quantitative deviations between theory and experiment appear at low pressure but without greatly affecting the giant diffusion effect.

We now consider the quantitative study of this stochastic nonequilibrium phenomenon. Figure 2 shows the time traces of the angular velocity $\dot{\varphi}$ obtained by short time Fourier transforms in the bistability region. In the locked state, the mean angular velocity is $\langle \dot{\varphi} \rangle_L \equiv 0$. While the mean rotational speed, $\langle \dot{\varphi} \rangle_R$, in the running state increases continuously with the pressure drop. The most noticeable feature of the time traces is the two-state noise-induced transitions, where the maximum of intermittency occurs in the middle of the bistability region at about $P \approx 0.56$ mbar [Fig. 1(b)].

We use the time traces of angular velocities to determine the mean occupation times in the locked and running states. Figure 3(a) shows the distributions $P(\tau/\langle\tau\rangle)$ of the mean occupation times, recorded for different gas pressures. These distributions decrease exponentially as expected for a Kramers-like problem. Deeper insight into two-state coexistence can be gained if we plot the pressure dependence of the average occupancy times in the locked and running states, as shown in Fig. 3(b), both for experimental

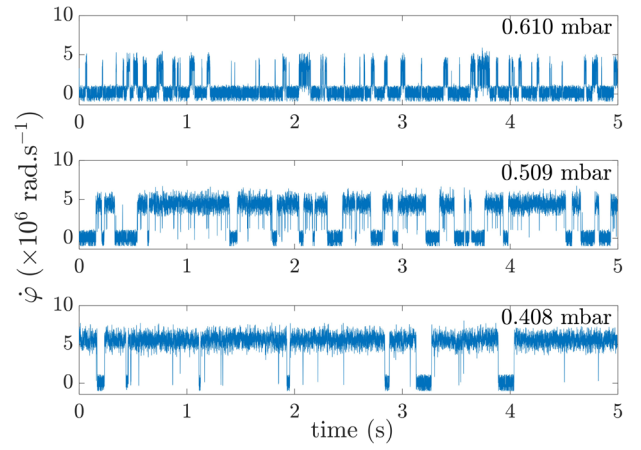


FIG. 2. Time traces of the dimer angular velocity $\dot{\varphi}$ obtained by short-time Fourier transform for the three pressures that are shown as gray horizontal curves in Fig. 1(b).

and numerical data. It can be evidenced that when $\Gamma_{\varphi} \ll \Omega_L$ (as in this case), the transition rate r_L out of a locked state (regardless of the final state, locked or running) is independent of the friction coefficient, i.e., of the pressure. This is in agreement with our observations [see Fig. 3(b) red squares and solid line]. Besides, this value is well approximated by the well-known Arrhenius law, $1/\tau_L = r_L \sim \Omega_L \exp(-E_b/k_B T)$, E_b being the barrier height given by the potential difference between a minimum and the lower neighboring maximum [42]. This offers insight into how a temperature change affects the stability of the torque state. A different behavior is observed for transitions from a running to a locked state for low damping and finite temperatures. This behavior is explained by the fact that the rate r_R is such that $1/\tau_R = r_R \sim \Gamma_{\varphi} \propto P$ [43]. Note that some differences occurring at low pressure can be observed

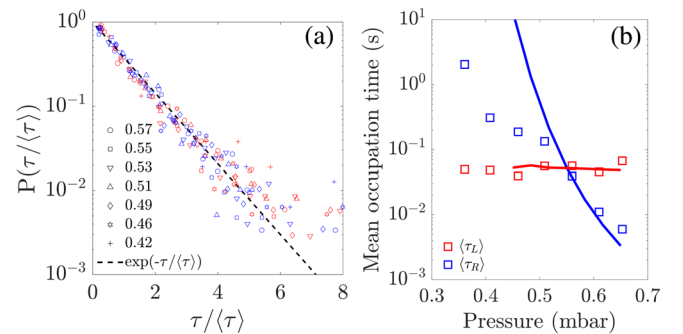


FIG. 3. (a) Probability distribution function of the occupation time from the locked to running states $P(\tau_L)$, red symbols, and the running to locked states $P(\tau_R)$, blue symbols, for various pressures where the bistability is observed. Exponential behaviors suggest that stochastic transitions between locked and running states are thermally activated, following an Arrhenius-type law. (b) Pressure dependence of the mean occupation times in the locked and running states [symbols: experiment, solid line: Langevin simulations, Eq. (2)].

between the one-dimensional model and the experiment [as seen in Fig. 3(b)]. They are not due to a time windowing effect, but could arise from the coupling between other rotational degrees of freedom, as seen below 0.45 mbar with the appearance of an additional resonance in the spectral densities [Fig. 1(b)].

In the rest of this Letter, we focus on the measurement of the effective rotational diffusion coefficient, which is defined by the Kubo relation

$$D_{\text{eff}} = \int_0^\infty dt' \langle [\dot{\varphi}(t') - \langle \dot{\varphi} \rangle][\dot{\varphi}(0) - \langle \dot{\varphi} \rangle] \rangle.$$

This coefficient satisfies the usual Einstein relation $\lim_{t \rightarrow \infty} \langle \varphi^2(t) \rangle - \langle \varphi(t) \rangle^2 = 2D_{\text{eff}}t$, where D_{eff} can in principle be enhanced by orders of magnitude over the free coefficient diffusion D_0 at the crossover from locked to running states. Interestingly, outside the region of bistability, the power spectral density of $\dot{\varphi}$ allows for a measurement of both $D_0 = k_B T / \Gamma_\varphi I_\perp$ and its related timescale $1/\Gamma_\varphi$. Surprisingly, we can derive a simple two-state stochastic noise model to fit our experimental results in the bistability region (see details in Sec. V.B of the Supplemental Material [17]). Since the parameter range we consider allows large timescale separations ($1/\Omega_R \ll 1/\Gamma_\varphi \ll \tau_L, \tau_R$), the spectral density of the rotation speed in the region of bistability reads

$$S_{\dot{\varphi}\dot{\varphi}}(\omega) = \frac{D_0}{1 + \frac{\omega^2}{\Gamma_\varphi^2}} + \frac{D_{\text{eff}}}{1 + \frac{\omega^2}{\Gamma_T^2}} \quad (3)$$

where $\Gamma_T = r_R + r_L$, is the total escape rate, corresponding to the longest timescale of the system. From the timetraces of the angular velocity $\dot{\varphi}$ (Fig. 2), we compute the power spectral densities of the rotation velocity (defined as the Fourier transform of the rotational velocity autocorrelation function) in the coexistence regime, as shown in Fig. 4(a). Using then Eq. (3), we can determine the effective diffusion D_{eff} relative to D_0 , that is displayed in Fig. 4(b) as a function of pressure. Note that Γ_φ and Γ_T are also measured, allowing us to corroborate the values of the nanodimer size and its aspect ratio. To go further into the two-state model, we use the transition rates r_R and r_L deduced from Fig. 3 to calculate D_{eff} . In our parameter regime, the two-state model gives an expression that bears much similarities with those developed in [11,44–46]

$$D_{\text{eff}} = \langle \dot{\varphi} \rangle_R^2 \frac{r_L r_R}{(r_L + r_R)^3}, \quad (4)$$

where $\langle \dot{\varphi} \rangle_R$ is the average angular velocity taken only over the running states of the whole temporal trace. Comparison of the filled and open circles in Fig. 4(b) indicates that when Eq. (4) is used with the results obtained from occupancy times, good agreement is obtained with the diffusion

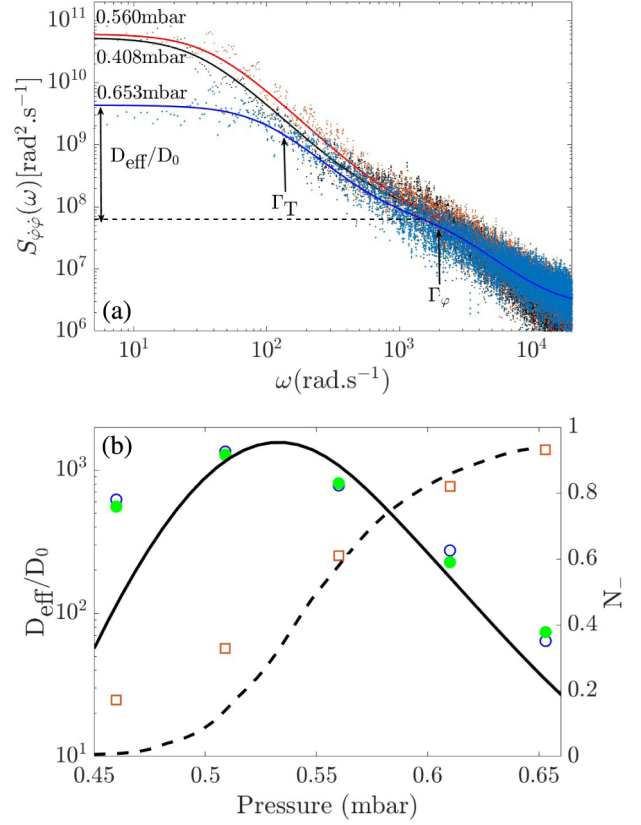


FIG. 4. (a) Measured power spectral densities of the dimer angular velocity (dots) and double Lorentzian fit [Eq. (3), solid curves] at the boundaries of the bistable region ($P = 0.653$ mbar in blue, $P = 0.408$ mbar in black), and at the pressure around which the maximum of giant diffusion exists ($P = 0.560$ mbar in red). The dashed line represents the free-space diffusion coefficient D_0 at $P = 0.653$ mbar, the double arrow displays the excess of diffusion D_{eff}/D_0 , while both the total escape rate Γ_T and the rotational damping rate Γ_φ are marked by vertical arrows. (b) On the left axis, Pressure dependence of the effective diffusion coefficient D_{eff} in units of D_0 estimated by two methods: (i) data from Fig. 4(a) are fitted by using Eq. (3), blue open circles, while (ii) transition rates obtained from Fig. 3 are used to calculate D_{eff} from Eq. (4), green filled circles. The black solid line results from the Langevin simulations [Eq. (2)]. On the right axis, Proportion of the mean occupancy in the locked state (red squares: experiment and black dashed line: Langevin simulations).

estimate by spectral densities by using Eq. (3). The occupancy rate in the locked state defined as $N_- = \langle \tau_L \rangle / (\langle \tau_L \rangle + \langle \tau_R \rangle)$ is represented by red squares in Fig. 4(b). We observe that the giant increase in the effective diffusion coefficient is roughly maximal at a pressure where the states are evenly distributed.

In conclusion, we have observed in a very small pressure range a giant increase of the diffusion coefficient in the underdamped and weak noise limit. Carefully calculating the optical torque, a reasonable quantitative agreement has been obtained using a one-dimensional Langevin model. This supports evidence that even though the real system

dynamics has six dimensions, it can be reduced to a one-dimensional system within at least some parameter regimes. Cooling the translational (and possibly rotational) degrees of freedom would mitigate the rotranslational coupling [15,16], enabling ideally over a wide parameter regime to reach the true one-dimensional Brownian nanorotor as described in Eq. (2). Thus, an optically levitated stator rotator constitutes an outstanding platform to study the issue of jump length distributions [47] and where its dynamics can be controlled down to the quantum ground state [48–50].

The authors acknowledge financial support from the Region Nouvelle-Aquitaine (Grant No. 2018-1R50304) and the Agence Nationale pour la Recherche (Grant No. ANR-21-CE30-0006). M. K. acknowledges the financial support from the EUR Light S&T Graduate Program (PIA3 Program “Investment for the Future,” ANR-17-EURE-0027).

*louis.bellando.physique@gmail.com

†yacine.amarouchene@u-bordeaux.fr

‡mathias.perrin@u-bordeaux.fr

§yann.louyer@u-bordeaux.fr

- [1] H. Kramers, Brownian motion in a field of force and the diffusion model of chemical reactions, *Physica (Amsterdam)* **7**, 284 (1940).
- [2] H. Risken, *The Fokker-Planck Equation: Methods of Solution and Applications Second Edition* (Springer, New York, 1989).
- [3] L. Longobardi, D. Massarotti, G. Rotoli, D. Stornaiuolo, G. Papari, A. Kawakami, G. P. Pepe, A. Barone, and F. Tafuri, Thermal hopping and retrapping of a brownian particle in the tilted periodic potential of a NbN/MgO/NbN Josephson junction, *Phys. Rev. B* **84**, 184504 (2011).
- [4] R. Hayashi, K. Sasaki, S. Nakamura, S. Kudo, Y. Inoue, H. Noji, and K. Hayashi, Giant Acceleration of Diffusion Observed in a Single-Molecule Experiment on F1-ATPase, *Phys. Rev. Lett.* **114**, 248101 (2015).
- [5] S. Strogatz, *Sync: The Emerging Science of Spontaneous Order* (Hyperion, New York, 2003).
- [6] J. W. M. Frenken and J. F. van der Veen, Observation of Surface Melting, *Phys. Rev. Lett.* **54**, 134 (1985).
- [7] S.-H. Lee and D. G. Grier, Giant Colloidal Diffusivity on Corrugated Optical Vortices, *Phys. Rev. Lett.* **96**, 190601 (2006).
- [8] M. Evstigneev, O. Zvyagolskaya, S. Bleil, R. Eichhorn, C. Bechinger, and P. Reimann, Diffusion of colloidal particles in a tilted periodic potential: Theory versus experiment, *Phys. Rev. E* **77**, 041107 (2008).
- [9] P. Reimann, C. Van den Broeck, H. Linke, P. Hänggi, J. M. Rubi, and A. Pérez-Madrid, Giant Acceleration of Free Diffusion by Use of Tilted Periodic Potentials, *Phys. Rev. Lett.* **87**, 010602 (2001).
- [10] G. Costantini and F. Marchesoni, Threshold diffusion in a tilted washboard potential, *Europhys. Lett.* **48**, 491 (1999).
- [11] B. Lindner and I. M. Sokolov, Giant diffusion of underdamped particles in a biased periodic potential, *Phys. Rev. E* **93**, 042106 (2016).
- [12] Y. Amarouchene, M. Mangeat, B. V. Montes, L. Ondic, T. Guerin, D. S. Dean, and Y. Louyer, Nonequilibrium Dynamics Induced by Scattering Forces for Optically Trapped Nanoparticles in Strongly Inertial Regimes, *Phys. Rev. Lett.* **122**, 183901 (2019).
- [13] M. Mangeat, Y. Amarouchene, Y. Louyer, T. Guerin, and D. S. Dean, Role of nonconservative scattering forces and damping on brownian particles in optical traps, *Phys. Rev. E* **99**, 052107 (2019).
- [14] L. Rondin, J. Gieseler, F. Ricci, R. Quidant, C. Dellago, and L. Novotny, Direct measurement of kramers turnover with a levitated nanoparticle, *Nat. Nanotechnol.* **12**, 1130 (2017).
- [15] J. Ahn, Z. Xu, J. Bang, Y.-H. Deng, T. M. Hoang, Q. Han, R.-M. Ma, and T. Li, Optically Levitated Nanodumbbell Torsion Balance and GHz Nanomechanical Rotor, *Phys. Rev. Lett.* **121**, 033603 (2018).
- [16] R. Reimann, M. Doderer, E. Hebestreit, R. Diehl, M. Frimmer, D. Windey, F. Tebbenjohanns, and L. Novotny, GHz Rotation of an Optically Trapped Nanoparticle in Vacuum, *Phys. Rev. Lett.* **121**, 033602 (2018).
- [17] See Supplemental Materials at <http://link.aps.org/supplemental/10.1103/PhysRevLett.129.023602>, which includes Refs. [18–32], for a complete description of our theoretical approach and the numerical methods used in the present paper. Detailed description of the experimental apparatus and also for the particle’s size and shape characterisation procedures are also provided.
- [18] C. Van den Broeck, Taylor dispersion revisited, *Physica (Amsterdam)* **168A**, 677 (1990).
- [19] L. Novotny and B. Hecht, *Principles of Nano-Optics* (Cambridge University Press, Cambridge, England, 2006).
- [20] E. Hebestreit, M. Frimmer, R. Reimann, C. Dellago, F. Ricci, and L. Novotny, Calibration and energy measurement of optically levitated nanoparticle sensors, *Rev. Sci. Instrum.* **89**, 033111 (2018).
- [21] P. V. Ruijgrok, N. R. Verhart, P. Zijlstra, A. L. Tchebotareva, and M. Orrit, Brownian Fluctuations and Heating of an Optically Aligned Gold Nanorod, *Phys. Rev. Lett.* **107**, 037401 (2011).
- [22] J. Gieseler, R. Quidant, C. Dellago, and L. Novotny, Dynamic relaxation of a levitated nanoparticle from a non-equilibrium steady state, *Nat. Nanotechnol.* **9**, 358 (2014).
- [23] A. Pinchuk and G. Schatz, Anisotropic polarizability tensor of a dimer of nanospheres in the vicinity of a plane substrate, *Nanotechnology* **16**, 2209 (2005).
- [24] H. Rudolph, J. Schäfer, B. A. Stickler, and K. Hornberger, Theory of nanoparticle cooling by elliptic coherent scattering, *Phys. Rev. A* **103**, 043514 (2021).
- [25] S. Albaladejo, R. Gómez-Medina, L. S. Froufe-Pérez, H. Marinchio, R. Carminati, J. F. Torrado, G. Armelles, A. García-Martín, and J. J. Sáenz, Radiative corrections to the polarizability tensor of an electrically small anisotropic dielectric particle, *Opt. Express* **18**, 3556 (2010).
- [26] J. G. Kirkwood and J. Riseman, The intrinsic viscosities and diffusion constants of flexible macromolecules in solution, *J. Chem. Phys.* **16**, 565 (1948).

- [27] B. Carrasco and J. Garcia de la Torre, Improved hydrodynamic interaction in macromolecular bead models, *J. Chem. Phys.* **111**, 4817 (1999).
- [28] B. Dahneke, Viscous resistance of straight-chain aggregates of uniform spheres, *Aerosol Sci. Technol.* **1**, 179 (1982).
- [29] R. A. Millikan, Coefficients of slip in gases and the law of reflection of molecules from the surfaces of solids and liquids, *Phys. Rev.* **21**, 217 (1923).
- [30] J. Gieseler, L. Novotny, and R. Quidant, Thermal nonlinearities in a nanomechanical oscillator, *Nat. Phys.* **9**, 806 (2013); M. Yoneda and K. Aikawa, Thermal broadening of the power spectra of laser-trapped particles in vacuum, *J. Phys. B* **50**, 245501 (2017).
- [31] J. Corson, G. W. Mulholland, and M. R. Zachariah, Calculating the rotational friction coefficient of fractal aerosol particles in the transition regime using extended kirkwood-riseman theory, *Phys. Rev. E* **96**, 013110 (2017).
- [32] D. A. Sivak, J. D. Chodera, and G. E. Crooks, Time step rescaling recovers continuous-time dynamical properties for discrete-time langevin integration of nonequilibrium systems, *J. Phys. Chem. B* **118**, 6466 (2014).
- [33] A. Ashkin and J. M. Dziedzic, Feedback stabilization of optically levitated particles, *Appl. Phys. Lett.* **30**, 202 (1977).
- [34] D. Hümmer, R. Lampert, K. Kustura, P. Maurer, C. Gonzalez-Ballester, and O. Romero-Isart, Acoustic and optical properties of a fast-spinning dielectric nanoparticle, *Phys. Rev. B* **101**, 205416 (2020).
- [35] G. D. Bruce, P. Rodríguez-Sevilla, and K. Dholakia, Initiating revolutions for optical manipulation: the origins and applications of rotational dynamics of trapped particles, *Adv. Phys. X* **6**, 1838322 (2021).
- [36] M. Rashid, M. Toroš, A. Setter, and H. Ulbricht, Precession Motion in Levitated Optomechanics, *Phys. Rev. Lett.* **121**, 253601 (2018).
- [37] B. A. Stickler, K. Hornberger, and M. S. Kim, Quantum rotations of nanoparticles, *Nat. Rev. Phys.* **3**, 589 (2021).
- [38] B. A. Stickler, B. Papendell, S. Kuhn, B. Schriniski, M. Millen, J. and Arndt, and K. Hornberger, Probing macroscopic quantum superpositions with nanorotors, *New J. Phys.* **20**, 122001 (2018).
- [39] J. Bang, T. Seberson, P. Ju, J. Ahn, Z. Xu, X. Gao, F. Robicheaux, and T. Li, Five-dimensional cooling and nonlinear dynamics of an optically levitated nanodumbbell, *Phys. Rev. Research* **2**, 043054 (2020).
- [40] Y. Arita, M. Mazilu, and K. Dholakia, Laser-induced rotation and cooling of a trapped microgyroscope in vacuum, *Nat. Commun.* **4**, 2374 (2013).
- [41] M. Nieto-Vesperinas, Optical torque: Electromagnetic spin and orbital-angular-momentum conservation laws and their significance, *Phys. Rev. A* **92**, 043843 (2015).
- [42] M. Büttiker and R. Landauer, Escape-energy distribution for particles in an extremely underdamped potential well, *Phys. Rev. B* **30**, 1551 (1984).
- [43] M. Büttiker, E. P. Harris, and R. Landauer, Thermal activation in extremely underdamped Josephson-junction circuits, *Phys. Rev. B* **28**, 1268 (1983).
- [44] S. Machlup, Noise in semiconductors: Spectrum of a two-parameter random signal, *J. Appl. Phys.* **25**, 341 (1954).
- [45] P. K. Ghosh, P. Hänggi, F. Marchesoni, F. Nori, and G. Schmid, Brownian transport in corrugated channels with inertia, *Phys. Rev. E* **86**, 021112 (2012).
- [46] C. W. Gardiner, *Handbook of Stochastic Methods for Physics, Chemistry and the Natural Sciences*, 3rd ed., Springer Series in Synergetics Vol. 13 (Springer-Verlag, Berlin, 2004), pp. xviii+415.
- [47] M. Borromeo, G. Costantini, and F. Marchesoni, Critical Hysteresis in a Tilted Washboard Potential, *Phys. Rev. Lett.* **82**, 2820 (1999).
- [48] U. Delic, M. Reisenbauer, K. Dare, D. Grass, V. Vuletic, N. Kiesel, and M. Aspelmeyer, Cooling of a levitated nanoparticle to the motional quantum ground state, *Science* **367**, 892 (2020).
- [49] L. Magrini, P. Rosenzweig, C. Bach, A. Deutschmann-Olek, S. G. Hofer, S. Hong, N. Kiesel, A. Kugi, and M. Aspelmeyer, Real-time optimal quantum control of mechanical motion at room temperature, *Nature (London)* **595**, 373 (2021).
- [50] F. Tebbenjohanns, M. L. Mattana, M. Rossi, M. Frimmer, and L. Novotny, Quantum control of a nanoparticle optically levitated in cryogenic free space, *Nature (London)* **595**, 378 (2021).

Giant diffusion of nanomechanical rotors in a tilted washboard potential

PACS numbers:

We describe in detail the experimental setup and how we synthesize the silica nano-dumbbells. We also present the configuration to follow in real time their orientation and the position of their center of mass. In particular, we explain the link between the orientation of the particle and the measured signal. Next, we present the data processing to obtain the angular velocity of the dumbbell and how we extract its effective diffusivity. We discuss how to evaluate the size and shape of the dimer using the translational degrees of freedom.

A theoretical part presents some results on the dynamics. First, we calculate the torque for an anisotropic Rayleigh particle, taking into account not only the extinction torque, but also the recoil (or scattering) contribution [1], in order to obtain a good quantitative agreement with the experiments. Finally, we derive the analytical expression for the low frequency behavior observed in the power spectral density (PSD) of the rotational speed. From the Langevin's equation, we get a general expression of the rotational effective diffusion coefficient, and explain why, with our parameters, the latter is identical to the effective diffusion coefficient given by a two-state telegraph noise model [2-4].

I. EXPERIMENTAL SETUP

A simplified scheme of the experimental setup is shown in Fig. 1. An axisymmetric particle (*i.e.*, a dumbbell composed of two silica nanospheres of diameter 140 ± 14 nm, $\rho = 2200$ kg.m⁻³ and refractive index $n = 1.45$) is trapped in an elliptically polarized laser beam at a wavelength of $\lambda = 1064$ nm. To do so, the linear polarization at the laser source output is oriented along the x axis by a half waveplate (HWP) plate. The polarization ellipticity is then set by a quarter waveplate (QWP), whose angle between the fast axis and x axis in the laboratory frame is $\phi_{\lambda/4}$.

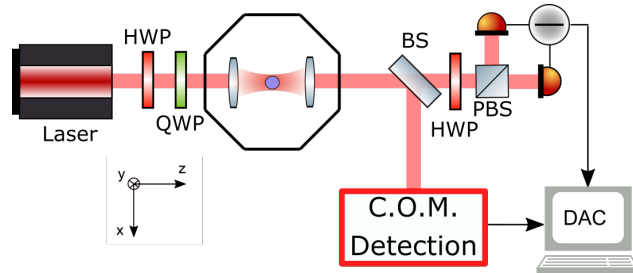


FIG. 1: Simplified top view scheme of the experimental apparatus. The 1064 nm laser light is focused in the vacuum chamber through a high numerical aperture microscope objective (N.A.= 0.8) and is then divided into two parts: one is sent on the detection system to measure the motion of the particle, the other part is analysed by a polarizer before to reach a balanced photodiode allowing a measurement of the orientation of the particle.

The laser source is an ultra stable and low noise continuous wave laser (AzurLight System) providing up to 7 W of optical power at a wavelength of $\lambda = 1064$ nm. Its relative intensity noise is of -150 dBc/Hz in the frequency range of interest (10 kHz to 100 MHz). The polarization stability ($< 0.1\%$) and the pointing fluctuations (< 0.5 μ rad for several hours) are minimized by using a polarizer with a high polarization extinction ratio and including the whole experiment in a box to prevent air fluctuations on the optical path.

The trapping beam is focused in the vacuum chamber by a high numerical aperture objective (Nikon IR Plan-APO : 0.8, W.D : 1mm) and recollected by an aspheric lens of numerical aperture 0.8. The transmitted beam from the trap is splitted in two: one half goes on the center of mass (COM) displacement detection setup, the other half goes on the setup for the detection of the particule orientation.

The COM detection is made by tracking in real time the extinction cross section of the nanoparticle, given by the

spatial integration of the interference pattern between the scattered field and the incident trapping field. For this part, we have used the same setup as in previous work, see [7], and figure 2.

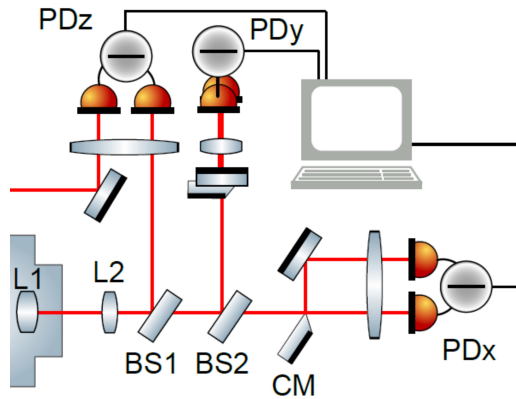


FIG. 2: Detailed top view of the scheme of the COM setup (BS, beam splitter, CM, D-cut mirror and PD, balanced photodiode).

The particle's center of mass displacement and its major axis orientation are recorded simultaneously at sampling rates varying between 10 MS/s to 200 MS/s, what permits to acquire temporal traces from 5 s to 100 s. The change of the gas pressure in the vacuum chamber modifies the damping of the particle's motion.

The nanoparticles (Microparticles GMBH) are loaded inside the vacuum chamber at atmospheric pressure by using a nebulizer (Omron Micro-Air), filled with a suspension of ethanol containing nanospheres. Nanodumbbells are formed by a proper dilution so that in average two nanospheres are contained in a single droplet. Once a particle is trapped, we evacuate the vacuum chamber from other diffusing nanoparticles.

II. MEASURED QUANTITIES OF THE ROTATIONAL DEGREES OF FREEDOM

A. Measurement of the dimer orientation and anisotropic polarizability

The light field arriving before the balanced photodiode is described as being the superposition of the field scattered by the particle and the reference field (Fig. 1). A simple analysis makes it possible to relate the differential intensity measured by the detectors to the orientation of the nanoparticle. The trapping beam is defined by

$$\mathbf{E}_{\text{inj}}(\mathbf{r}) = E_0(\mathbf{r})e^{i\eta(\mathbf{r})} \begin{pmatrix} \cos(\phi_{\lambda/4}) \\ i \sin(\phi_{\lambda/4}) \\ 0 \end{pmatrix}, \quad (1)$$

where $E_0(\mathbf{r})$ and $\eta(\mathbf{r})$ are the Gaussian beam amplitude and phase [9, 10], $\delta = 2\phi_{\lambda/4}$ is the beam ellipticity.

The orientation of the dimer is given by its director axis $\hat{n} = [\cos \varphi \sin \theta; \sin \varphi \sin \theta; \cos \theta]$, expressed in the laboratory frame ($\mathbf{e}_x, \mathbf{e}_y, \mathbf{e}_z$), with usual polar and azimuthal angles.

The polarizability matrix, $\underline{\alpha}$, is diagonal in the dimer's eigenframe, and has two components α_{\perp} , twice degenerated, and α_{\parallel} . Their value can be estimated analytically [11-13] or computed numerically. This analysis leads to the real and imaginary parts of the polarizability: $\alpha'_{\perp, \parallel}$ and $\alpha''_{\perp, \parallel}$, respectively. In the laboratory frame, the polarizability matrix and the vectorial electric dipole moment for any orientation is given by

$$\underline{\alpha} = \alpha_{\perp} \mathbb{I} + (\alpha_{\parallel} - \alpha_{\perp}) \hat{n} \hat{n}, \quad (2)$$

$$\mathbf{p} = \underline{\alpha} \mathbf{E}_{\text{inj}}, \quad (3)$$

where \mathbb{I} is the identity matrix and $\hat{n} \hat{n}$ the dyadic product.

The forward scattered field, \mathbf{E}_s , in a direction \mathbf{r}_L towards the collecting lens, depends on the dipole moment of the particle, see Eq. (3) in which one uses the far-field Green tensor [5 Eq. (8.52) and Eq. (8.61)]. By evaluating the modulated intensity received by the photodiode on each polarization channel (along x or along y) as $E_{\text{inj}, x, y} \cdot E_{s, x, y}^* + E_{\text{inj}, x, y}^* \cdot E_{s, x, y}$, and integrating on \mathbf{r}_L , we can write the differential intensity that is measured.

Assuming the dimer is in the (x,y) plane, *i.e.* $\theta = \pi/2$, and the half-waveplate is adjusted so that the signal averaged over positions of the dimer is perfectly balanced, we obtain a simple expression for the differential voltage $r(t)$, proportional to the intensity difference :

$$r(t) \propto \frac{E_0^2}{2} \left((\alpha_{\parallel}'' - \alpha_{\perp}'') \sin(\delta) \cos[2\varphi(t)] + (\alpha_{\parallel}' - \alpha_{\perp}') \sin[2\varphi(t)] \right). \quad (4)$$

In practice, the measured signal is a nonlinear function of the dimer orientation. To understand the link between the signal spectrum and the characteristic frequencies of the problem, it is interesting to consider a limiting case. In the absence of noise, let us take the following ansatz for the temporal evolution of the orientation of the particle

- $\varphi(t) = \Omega_R t$, when the particle spins,
- $\varphi(t) = \varphi_{eq} + \varphi_0 \cos(\Omega_L t)$, when the particle is in the torsional state around an equilibrium position φ_{eq} .

Therefore, in the rotational state, the signal would peak at the frequency $2\Omega_R$, while, for the torsional state, the expansion of $\sin[2\varphi(t)]$ and $\cos[2\varphi(t)]$ would give a signal frequency at Ω_L , followed by their harmonics.

In the presence of thermal noise, we observe both experimentally and numerically the presence of the peak of rotation in the spectral density at $2\Omega_R$, and several peaks associated with the torsional state (both fundamental and harmonics, see fig. 1 of the main text). However, it is difficult to say if the experimental peaks are really harmonics of the 1D problem, or come from the hybridization of the φ motion with the other angles, or even from the coupling with the degrees of freedom in translation.

III. TREATMENT PROCEDURES FOR LOCAL ANGULAR FREQUENCY EVALUATION AND TRANSIT TIME EXTRACTION

In this section, we present our data processing to evaluate the instantaneous angular vibration of the trapped nanodumbbell and how we extract the transit times to calculate the effective diffusion constant.

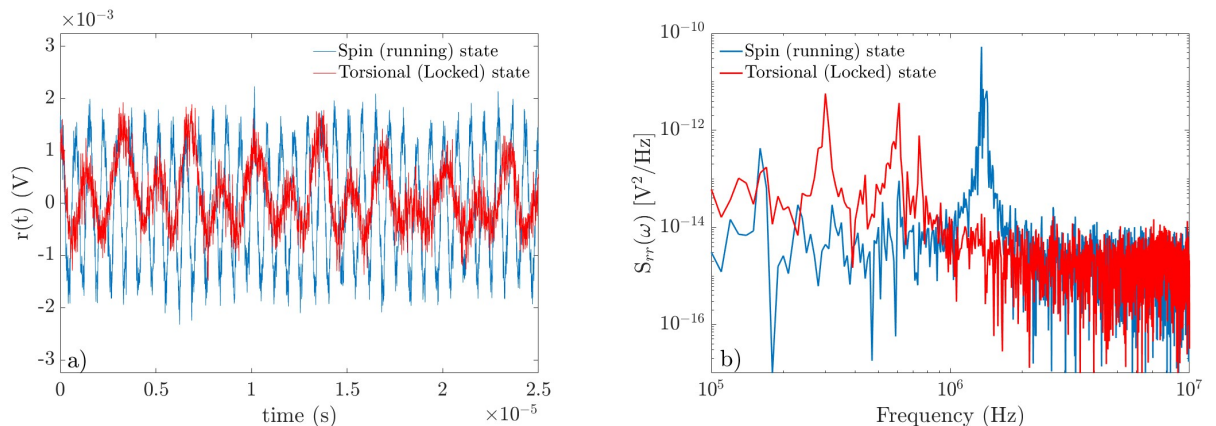


FIG. 3: **a)** Measured signal $r(t)$ corresponding to the angular motion $\varphi(t)$ for a gas pressure $P = 0.56$ mbar, when the particle is in the locked (torsional) state (red curve) or in the running (spinning) state (blue curve). **b)** Measured Power Spectral Densities obtained from the temporal trace presented in **a)**.

Changes in the polarization of the transmitted beam are related to changes in the instantaneous orientation of the trapped particle, which are recorded by a well-balanced photodiode. This signal is formed by time traces of 5 to 100 seconds. We divide them into subtraces whose length varies between $50 \mu\text{s}$ to 1 ms in order to evaluate the instantaneous angular velocity. For each subsample, we then calculate the one-sided power spectral density, which reads as

$$S_{rr}(\omega) = \int_0^{\infty} dt \left\langle [r(t) - \langle r(t) \rangle] [r(0) - \langle r(0) \rangle] \right\rangle e^{i\omega t} \quad (5)$$

Figure 3 shows the measured signals (left panels) and their corresponding spectra (right panels), when the particle is in the locked or rotating state, both at a pressure of 0.560 mbar. Each PSD was calculated for a time window of 100 μ s. This permits to reconstruct the time trace of angular frequency.

IV. DAMPING IN TRANSLATION AND ROTATION AND CHARACTERIZATION OF THE SIZE AND SHAPE OF THE PARTICLE

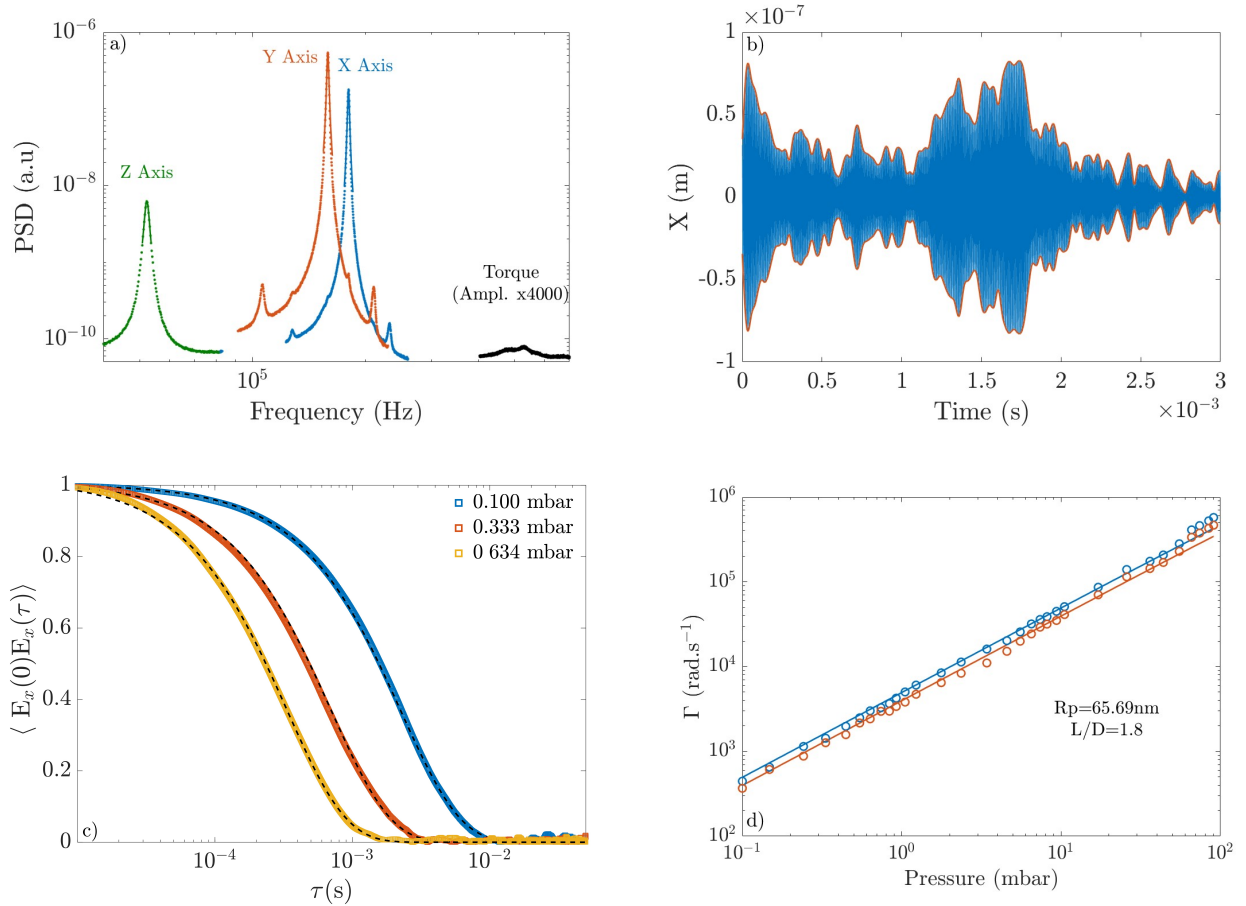


FIG. 4: **a)** Measured Power Spectral Density of the translation and torsional motion of the trapped nanodumbbell at a pressure of $P = 1.53$ mbar averaged over a time period of 20 s. **b)** Time trace of the particle motion in translation along the x axis from which is extracted the slowly varying envelope (red curves). **c)** Energy autocorrelation for various pressures ranging from 0.1 to 0.634 mbar. The dashed lines represent a fit by an exponential decay. **d)** Translational damping rates of the nanodimer along the direction of its main axis (\perp , in blue) and perpendicular to it (\parallel , in red), as a function of the gas pressure. Symbols are measured values, solid lines are fitted from Eq. (8). The constant difference between the damping rates proves that the trapped object is an asymmetric particle and that, in the long-time averages, the friction of the translation degrees is not affected by the type of angular motion (torsional or rotational regime).

A. Determination of translational damping and particle geometry

The shape and size of the particle are determined under linear polarization of the trapping beam using different standard [6] and nonlinear [7] calibration techniques.

Figure 4 shows the experimental results on the translational degrees of freedom. In the high pressure regime, we extract the widths Γ_i of the PSDs by fitting the Lorentzian lineshape on the three axis, see figure 4(a). At low

pressures, nonlinearities smear the narrow Lorentzian shape of the PSDs [7]. To circumvent this issue, we extract both the time-varying local frequency and position from the slowly varying envelope of the position signals along an axis [Fig. 4(b)]. This allows a measurement of the time-resolved energy of the mechanical oscillator. Then, from the correlation function in energy [Fig. 4(c)] decreasing exponentially, we infer the characteristic time which corresponds to the inverse of damping rate. This amounts to consider

$$E_i(t) = \frac{m\Omega_i^2(t)x_i^2(t)}{2}, \quad (6)$$

the time-resolved energy, whose correlations decreases exponentially as

$$\langle E_i(0)E_i(\tau) \rangle \propto e^{-\Gamma_i\tau}.$$

Fitting the results of figure 4(c), we obtain Γ_i .

In practice, the main axis of the nanodimer is oriented in the direction of the linear polarization (in the low temperature limit), lying in the (\hat{x}, \hat{y}) plane. This permits to infer Γ_{\parallel} and Γ_{\perp} , the damping rates corresponding to the dimer motion in the eigenframe, along its main axis, and perpendicular to it. Figure 4(d) shows their values as a function of pressure. Given the dimer geometrical cross sections, we logically recover that $\Gamma_{\perp} > \Gamma_{\parallel}$. From these results, we can deduce the particle size and shape.

We first evaluate the parallel and perpendicular hydrodynamic drag coefficients in the continuous regime, $\gamma_{\perp, \parallel} = m\Gamma_{\perp, \parallel}$, where m is the mass of the dumbbell, with the help of the Kirkwood-Reisemann theory [14, 15], and write

$$\mu_{\perp, \parallel} = \frac{\gamma_{\perp, \parallel}}{\gamma_S}, \quad (7)$$

where, $\mu_{\perp, \parallel}$ are the coefficient of the mobility tensor, and $\gamma_S = 6\pi\eta R_p$, where η is the fluid viscosity in the continuous limit (at room pressure) and R_p the radius of one sphere of the dumbbell. Note that we consider the two spheres to be identical.

Then, to evaluate the sphere radius and the dimer's aspect ratio L/D , L being the total length in \parallel direction, and $D = 2R_p$, the diameter of a sphere, we consider the behaviour of both perpendicular and parallel damping rates as a function of the pressure P . For a single sphere, the damping rate can be expressed in terms of Knudsen number $Kn = \lambda_{\text{mfp}}/R_p$, where we introduce the mean free path of air molecules $\lambda_{\text{mfp}} = \lambda_0 P_{\text{atm}}/P$, with $\lambda_0 = 68$ nm. For an aggregate of N spheres (here, $N = 2$), different effective Knudsen numbers $Kn_{a, \parallel} = 1.23Kn$ (resp., $Kn_{a, \perp} = 1.39Kn$) is used along the parallel (resp. perpendicular) directions [16]. Finally, the damping rates are obtained as a function of the gas pressure

$$\Gamma_{\perp, \parallel}(P) = C_a^{-1}(Kn_a)\gamma_{\perp, \parallel}/m, \quad (8)$$

where we have used a slip correction factor corresponding to the modified Millikan's formula [17]

$$C_a(Kn_a) = 1 + Kn_a \left[A + B \exp\left(-\frac{C}{Kn_a}\right) \right], \quad (9)$$

with $A = 1.234$, $B = 0.404$ and $C = 0.876$ the coefficients that Millikan has obtained for a single sphere in the rarefied gas regime. Asymptotically, considering a dimer such that $L/D = 2$, one recovers for the damping rates ratio the values 1.13 in the continuous regime ($Kn_a \rightarrow 0$) and 1.26 in the rarefied regime ($Kn_a = 100$) [19].

B. Determination of the rotational damping rate

Using the instantaneous rotation frequency (obtained by short-time Fourier transform methods), we calculate the spectral density of the rotational frequency and fit it using Eq. (19) that has been obtained from the Ornstein-Uhlenbeck theory, see Sec. (V B). This procedure allows to deduce the rotational damping rate Γ_{φ} at any pressure. Figure 5 shows such an example at 0.225 mbar with a rotational damping rate of $\Gamma_{\varphi}/2\pi = 143$ Hz.

To confirm the estimated size of the beads and the aspect ratio obtained from the damping rates on the translational degrees of freedom, we plot the measured rotational damping rate as a function of the gas pressure. From the estimated size of the beads and the aspect ratio L/D obtained from the translational damping rate, we take from ref. [19] the rotational damping rate normalized by the rotational damping rate of the unit sphere ($\Gamma_{\varphi, \text{Sphere}} = 8\pi\eta R_p^3/I_{\text{Sphere}}$).

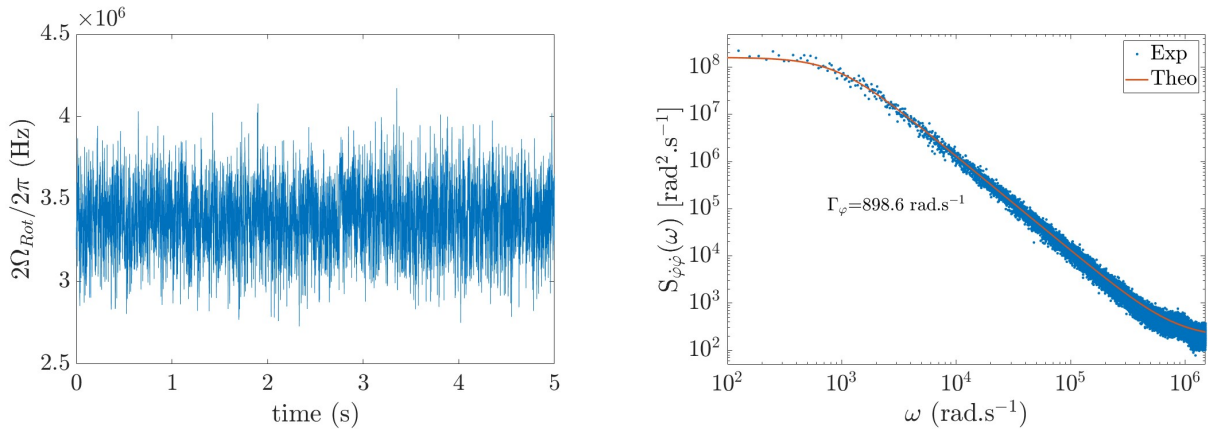


FIG. 5: **a)** Temporal trace of the rotation frequency at 0.225 mbar. **b)** PSD of the rotation pulsation for the same experimental parameter as **a)**. The extraction of the cut-off frequency allows a measurement of the rotational damping rate of the particle.

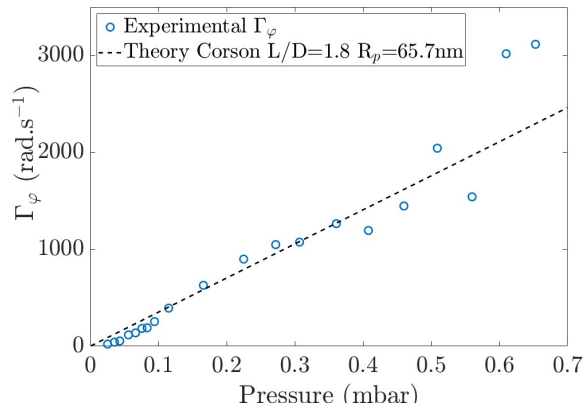


FIG. 6: Evolution of the rotational damping rate Γ_φ as a function of the gas pressure. The dotted line represents the theoretical damping rate on the rotational degrees of freedom.

In the case of an aggregate of N spheres, the rotational damping rate can be expressed via a correction slip factor and the rotational damping rate of a single sphere as

$$\Gamma_{\varphi, \text{Dumbbell}} = C_n \Gamma_{\varphi, \text{Sphere}}. \quad (10)$$

From [19, figure 4], we extract the rotational drag torque in units of the rotational drag torque of the elementary sphere for an aspect ratio L/D of a given particle using the fitted formula

$$C_n = 3.62 - 6.97 \frac{L}{D} + 4.37 \left(\frac{L}{D} \right)^2. \quad (11)$$

Figure 6 shows the measured damping rates for the rotation and the good agreement with the theoretical formulas given by Eqs. (10) and (11) for an aspect ratio $L/D = 1.8$ and with radii of 65.7 nm.

V. DYNAMICS OF THE DIMER ORIENTATION

A. Expression of the optical torque and equation of the rotational motion for an axisymmetric anisotropic dielectric particle

The torque due to the field-dipole interaction is [1]

$$\vec{M} = \left[\frac{1}{2} \text{Re}(\mathbf{p} \times \mathbf{E}_{\text{inj}}^*) \right] + \left[\frac{k^3}{12\pi\epsilon_0} \text{Im}(\mathbf{p} \times \mathbf{p}^*) \right], \quad (12)$$

where we take into account both the extinction and scattering contribution to the total torque – respectively corresponding to first and second term in brackets, Eq. (12).

In the particular case where the dimer is perpendicular to the beam axis, $\theta = \pi/2$, and $\vec{M} = M\mathbf{e}_z$. The optical torque is then given by

$$M = M_C - M_L \sin(2\varphi), \quad (13)$$

$$M_C = \frac{|E_0(\mathbf{r})|^2}{2} \left[\frac{\alpha''_{\parallel} + \alpha''_{\perp}}{2} - \frac{k^3}{6\pi\epsilon_0} (\alpha''_{\parallel}\alpha''_{\perp} + \alpha'_{\parallel}\alpha'_{\perp}) \right] \sin \delta, \quad (14)$$

$$M_L = \frac{|E_0(\mathbf{r})|^2}{2} \left[\frac{\alpha'_{\parallel} - \alpha'_{\perp}}{2} + \frac{k^3}{6\pi\epsilon_0} (\alpha''_{\parallel}\alpha'_{\perp} - \alpha'_{\parallel}\alpha''_{\perp}) \right] \cos \delta. \quad (15)$$

In Eq. (13), the first term, M_C , does not depend on the dimer orientation, and has a maximum value for circularly polarized light. It describes the torque transfer via absorption and the finite-size effect of the scatterer. Note that M_C is strictly zero for a non-absorbing spherical Rayleigh particle, as extinction and scattering contributions cancel out [1]. It is however slightly non zero for, e.g., a non-absorbing nanodimer, or slightly ellipsoidal nanoparticle.

The second term, $-M_L \sin(2\varphi)$, is of maximum amplitude for linearly polarized light, and is also related to the geometric asymmetry of the dimer. Within the limit of small angles, it is reduced to a restoring torque, around the equilibrium position defined by $M(\varphi_{eq}) = 0$.

While the scattering torque is generally negligible for lossy Rayleigh particles that have large α'' , it must absolutely be taken into account here, as it induces a drop of roughly an order of magnitude for M_C . This makes it possible to obtain a numerical value of the rotation frequency at low pressure in agreement with the experiment (see figure 1(b) in the main text).

We have computed numerically the complex polarizabilities α_{\parallel} and α_{\perp} for the dimer of the experiment, with a Finite Element Method (FEM), Comsol Multiphysics. To tackle the convergence problems of FEM, we have first solved the Maxwell equations for a dimer made of non-overlapping spheres, for which one can use a very accurate method, based on the decomposition of electric fields on spherical harmonics. The results we obtained are in very good agreement with FEM simulations, when we use improved meshes and boundary conditions for the FEM. We typically obtain a 1 % mismatch between both methods, on the electric dipole moment $\mathbf{p} \equiv \int_{\text{Dimer}} \epsilon_0(\epsilon_r - 1)\mathbf{E}dV$. We then used this FEM for a dimer with the same size and aspect ratio as those measured, see Sec. (IV), made of overlapping spheres. \mathbf{p} has been computed, and the polarizabilities $\alpha_{\perp, \parallel}$ were inferred from Eq. (3). Then, M_C and M_L are computed from Eq. (14) (15).

Note that we allowed slight changes in the dimer geometry (departing not more than 5% from the measured values of D and L/D), so as to obtain a value of M_C that gives the best agreement with experimental results, (fig. 1(b) in the main text). The torque M_C is indeed evaluated as the difference of two terms that have a close value, see inside the brackets of Eq. (14), and is therefore very sensitive to numerical inaccuracies on $\alpha''_{\parallel, \perp}$.

Our approach, using Eq. (14), considerably improves the numerical evaluation of the frequency of rotation in the regime of low pressures.

Finally, the equation of motion for the degree of freedom in rotation around the optical axis is described by a Langevin equation

$$I_{\perp} \ddot{\varphi} = -\Gamma_{\varphi} I_{\perp} \dot{\varphi} + M(\varphi) + \xi(t), \quad (16)$$

where $M(\varphi) = M_C - M_L \sin(2\varphi)$. I_\perp represents the inertia moment around the optical z axis, Γ_φ is the rotational damping and $\xi(t)$ is a centered Gaussian noise, such as $\langle \xi(t_1)\xi(t_2) \rangle = 2\Gamma_\varphi I_\perp k_B T \delta(t_2 - t_1)$. We used the Sivak algorithm [23] to compute the time traces.

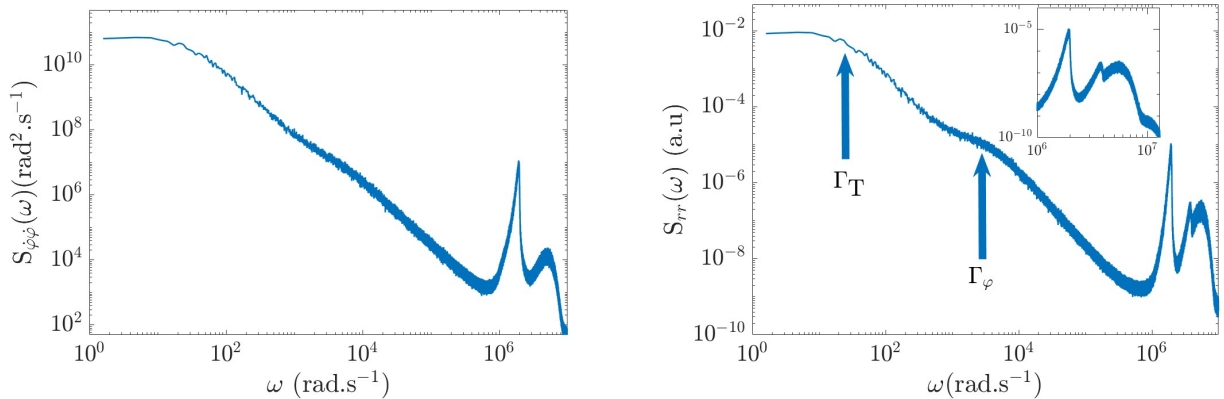


FIG. 7: Calculated Power Spectral Densities for both quantities $\dot{\varphi}$, panel (a) and $r(t)$, panel (b), at the maximum of superdiffusion peak, under elliptical polarisation ($\phi_{\lambda/4} = 25^\circ$). Relatively good agreement with experimental results (see panel (a) and Fig. 4(a) of the main text) is obtained. The characteristic frequencies Γ_T and Γ_φ are shown by arrows on panel (b). The inset, on panel (b) displays the fundamental and harmonics of the torque signal (the three low frequency peaks) as well as the spin peak (the highest frequency bump).

B. Low-frequency behaviour of the PSD : a superdiffusion

The goal is to calculate the correlation function of the rotational speed in the bistable regime, to then obtain the power spectral density of the rotational speed and the effective diffusion coefficient of the rotation. We start with [2]:

$$S(t) = \left\langle [\dot{\varphi}(t) - \langle \dot{\varphi}(t) \rangle] [\dot{\varphi}(0) - \langle \dot{\varphi}(0) \rangle] \right\rangle \quad (17)$$

Consider first that $M_L = 0$, *i.e.* the trapping beam is circularly polarized. Then, one observes from Eq. (16) that $\varphi(t) - \frac{M_C}{I_\perp \Gamma_\varphi} t$ is an Ornstein-Uhlenbeck (O.U.) process. In such case, as $\dot{\varphi}$ is simply shifted by a constant, we find the relation known for the O.U. process:

$$\left\langle [\dot{\varphi}(t_1) - \langle \dot{\varphi}(t_1) \rangle] [\dot{\varphi}(t_2) - \langle \dot{\varphi}(t_2) \rangle] \right\rangle = \frac{k_B T}{I_\perp} e^{-\Gamma_\varphi |t_2 - t_1|} \quad (18)$$

Using Eq. (5), we obtain

$$S_{\dot{\varphi}, \dot{\varphi}}(\omega) = \frac{1}{2} \int_{-\infty}^{\infty} S(t) e^{i\omega t} dt = \frac{k_B T}{I_\perp} \frac{\Gamma_\varphi}{\omega^2 + \Gamma_\varphi^2} \quad (19)$$

Eq. (19) has been used to fit the experimental data of figure 5 obtained in the spin state.

At zero frequency, we obtain the diffusion coefficient for angular frequency in a spin state, which is identical to the free space diffusion

$$D_o = \frac{k_B T}{\Gamma_\varphi I_\perp}. \quad (20)$$

We now consider the general case for a washboard potential.

Starting from the equation of motion, and integrating between 0 and t . One obtains

$$\dot{\varphi}(t) = \dot{\varphi}(0) e^{-\Gamma_\varphi t} + \int_0^t \frac{1}{I_\perp} M[\varphi(u)] e^{-\Gamma_\varphi(t-u)} du + \int_0^t \frac{\xi(u)}{I_\perp} e^{-\Gamma_\varphi(t-u)} du. \quad (21)$$

As $M_L \neq 0$, extra time dependant contributions have to be considered to calculate $S(t)$. For a given time t , we consider all the times $0 < t_1 < t_2 < \dots < t_N < t$ that correspond to a change of state (from spin to torque or from torque to spin). Integrals of the following type will now contribute to $\langle \dot{\varphi}(t)\dot{\varphi}(0) \rangle$:

$$\left\langle \dot{\varphi}(0) \int_{t_i}^{t_{i+1}} \frac{1}{I_\perp} M[\varphi(u)] e^{-\Gamma_\varphi(t-u)} du \right\rangle, \quad (22)$$

in which the state of $\varphi(u)$ is purely torquing or purely spinning. For large times, $\varphi(u)$ and $\dot{\varphi}(0)$ are uncorrelated, and upon averaging, $\langle M[\varphi(u)] \rangle$ appears in the contribution to $\langle \dot{\varphi}(t)\dot{\varphi}(0) \rangle$. But, when the particule torques, $\langle M[\varphi(u)] \rangle = 0$. Finally, the torque states do not contribute to $\langle \dot{\varphi}(t)\dot{\varphi}(0) \rangle$.

Let's now consider only the intervals $[t_i..t_{i+1}]$ where the particle continuously rotates. Their contribution to $\langle \dot{\varphi}(t)\dot{\varphi}(0) \rangle$, can be rewritten as

$$\left\langle \dot{\varphi}(t)\dot{\varphi}(0) \right\rangle = \sum_i I_{S_i} = \sum_i \left\langle \dot{\varphi}(0) \right\rangle \left\langle \int_0^{t_{i+1}-t_i} \frac{1}{I_\perp} M[\varphi(t_i+v)] e^{\Gamma_\varphi v} e^{-\Gamma_\varphi(t-t_i)} dv \right\rangle, \quad (23)$$

where the random variable $t_{i+1} - t_i$ has an exponential law of mean time τ_R , independantly of the starting time t_i . Taking the average on $t_{i+1} - t_i$, one obtains

$$I_{S_i} = \left\langle \dot{\varphi}(0) \right\rangle \int_0^\infty \frac{e^{-\tau/\tau_R}}{\tau_R} d\tau \int_0^\tau \frac{1}{I_\perp} \left\langle M(\varphi(t_i+v)) \right\rangle e^{\Gamma_\varphi v} e^{-\Gamma_\varphi(t-t_i)} dv \quad (24)$$

Further computation based on the timescale separation between damping and rotation : $1/\Gamma_\varphi$ and $1/\Omega_{\text{Rot}}$ shows that averaging on the possible values of $\varphi(t_i)$ cancels the modulated term in M :

$$\left\langle M(\varphi(t_i+v)) \right\rangle = M_C$$

We notice that the spin contributions at the different t_i will have the same value, except for the coefficient $\exp(-\Gamma_\varphi(t-t_i))$. Then, the only non-negligible contribution is the last one, between t_N and t , when the dynamics ends in spin state. If the particle would end in torque state, the contribution to time correlation function would not be the one from the last state (between t_N and t) but the former one, between t_{N-1} and t_N , whose contribution is weighted by an $\exp(-\Gamma_\varphi \tau_L)$ coefficient, and then negligible, in our problem where $1/\Gamma_\varphi \ll \tau_L$. This point was discussed in ref. [4], where no damping was considered, and can now be generalized to a washboard dynamics, Eq. [16], due to the timescale separation between $1/\Gamma_\varphi$ and τ_L .

To go on, let us denote P_N the probability to end in spin state, knowing one starts in spin state. Considering only this main contribution :

$$\left\langle \dot{\varphi}(t)\dot{\varphi}(0) \right\rangle = P_N \left\langle \dot{\varphi}(0) \right\rangle \left\langle \int_0^{t-t_N} \frac{M_C}{I_\perp} e^{\Gamma_\varphi v} e^{-\Gamma_\varphi(t-t_N)} dv \right\rangle. \quad (25)$$

In the long time limit, $t - t_N$ has a uniform law between 0 and τ_R . We obtain immediatly, as $\tau_R \gg 1/\Gamma_\varphi$:

$$\left\langle \dot{\varphi}(t)\dot{\varphi}(0) \right\rangle = P_N \left\langle \dot{\varphi}(0) \right\rangle \frac{M_C}{\Gamma_\varphi I_\perp}. \quad (26)$$

Therefore, the only non negligible contributions to $\langle \dot{\varphi}(t)\dot{\varphi}(0) \rangle$ occur when the particule starts in spin state and ends in spin state.

The probability to end in spin state, knowing that we start in spin state (so as to have $\langle \dot{\varphi}(0) \rangle \neq 0$) is the probability to make an even number of transitions. Borrowing from [4] Eq. (6)], it reads

$$P_N = \frac{1}{\tau_R + \tau_L} \left[\tau_L e^{-t/T} + \tau_R \right] \quad (27)$$

where $1/T = 1/\tau_R + 1/\tau_L$, and considering that $S(t) = S(-t)$, one obtains :

$$\langle \dot{\varphi}(t)\dot{\varphi}(0) \rangle = \frac{k_b T}{I_\perp} e^{-\Gamma_\varphi |t|} + \frac{M_C}{\Gamma_\varphi I_\perp} \langle \dot{\varphi}(0) \rangle \frac{1}{\tau_R + \tau_L} \left[\tau_L e^{-|t|/T} + \tau_R \right] \quad (28)$$

By ergodicity :

$$\langle \dot{\varphi}(0) \rangle = \frac{\tau_R}{\tau_R + \tau_L} \langle \dot{\varphi} \rangle_R,$$

where $\langle \dot{\varphi} \rangle_R$ is the spinning frequency averaged only on spinning events of the temporal trace, at the pressure considered. This frequency can be measured experimentally. Besides, the coefficient $\frac{M_C}{\Gamma_\varphi I_\perp}$ can be evaluated using the mobility μ in the spinning state [22] :

$$\langle \dot{\varphi} \rangle_R = \Gamma_\varphi \mu \frac{M_C}{\Gamma_\varphi I_\perp}$$

So that the PSD is :

$$S_{\dot{\varphi}, \dot{\varphi}}(\omega) = D_o \frac{1}{1 + \left(\frac{\omega}{\Gamma_\varphi}\right)^2} + D_{\text{eff}} \frac{1}{1 + \left(\frac{\omega}{\Gamma_T}\right)^2} \quad (29)$$

with

$$D_{\text{eff}} = \left[\Gamma_\varphi \mu \right] \left(\frac{M_C}{\Gamma_\varphi I_\perp} \right)^2 \frac{r_R r_L}{(r_R + r_L)^3}, \quad (30)$$

where $r_R = 1/\tau_R$ (resp. $r_L = 1/\tau_L$).

The formula Eq. (29) has been used to fit the experimental data in the main text.

Computing the values in the spinning state (e.g. at 0.3 mbar), in Risken notation [22], we obtain

$$\begin{aligned} \Theta/d &\equiv 4k_b T / (2M_L) = 0.12 \\ F_o/\sqrt{d} &\equiv \frac{2M_C}{I_\perp \Gamma_\varphi} \sqrt{\frac{I_\perp}{2M_L}} = 7.5 \end{aligned}$$

Thus, we notice from [22] Fig. (11.30)], that the mobility in the spin state part of the temporal trace is $\Gamma_\varphi \mu \sim 1$.

Consequently, with our experimental parameters, we recover the expression given by the “two-state” theory toy model [2, 3]. The coefficient $\frac{M_C}{\Gamma_\varphi I_\perp}$ is evaluated from the experimental data, as the slope of $\langle \dot{\varphi} \rangle_R$ versus $1/\Gamma_\varphi$, in the low pressure spin state.

At first sight, the fact that the washboard giant diffusion, on a particle that undergoes forcing, damping and non-linear oscillations can be described by a toy model with 2 static states (and no dynamics) may seem surprising. Starting from the equation of motion, we have shown that this is due to the strong time scale separation between rotation ($1/\Omega_{\text{Rot}}$), damping ($1/\Gamma_\varphi$), and lifetime of the 2 states, τ_R, τ_L . It could be interesting, in further works, to study the deviations to the 2-state model, when the timescale separation blurs out.

[1] M. Nieto-Vesperinas, Phys. Rev. A **92**, 043843 (2015).

- [2] Benjamin Lindner and Igor M. Sokolov, *Phys. Rev. E* **93**, 042106 (2016)
- [3] C. Van der Broeck, *Physica A*. **168**, 677 (1990)
- [4] S. Machlup, *J. Appl. Phys.* **25**, 341 (1954).
- [5] L. Novotny, B. Hecht, “Principles of Nano-optics”, 2nd edition, Cambridge (2012).
- [6] E. Hebestreit, M. Frimmer, R. Reimann, C. Dellago, F. Ricci, L. Novotny, *Rev. of Sci. Inst.* **89**, 033111 (2018).
- [7] Y. Amarouchene, M. Mangeat, B. V. Montes, L. Ondic, T. Guérin, D. S. Dean, and Y. Louyer, *Phys. Rev. Lett.* **122**, 183901 (2019).
- [8] P. V. Ruijgrok, N. R. Verhart, P. Zijlstra, A. L. Tchebotareva, and M. Orrit, *Phys. Rev. Lett.* **107**, 037401 (2011).
- [9] Jan Gieseler, Lukas Novotny, Romain Quidan, *Nature Nanotech.* **9**, 806–10 (2013).
- [10] M. Mangeat, Y. Amarouchene, Y. Louyer, T. Guérin and D. S. Dean, *Phys. Rev. E* **99**, 052107 (2019).
- [11] A. Pinchuk, G. Schatz, *Nanotech.* **16**, 2209-2217 (2005).
- [12] H. Rudolph, J. Scäfer, B. A. Stickler, K. Hornberger, *Phys. Rev. A*. **103**, 043514 (2021).
- [13] S. Albaladejo, R. Gomez-Medina, L. S. Froufe-Perez, H. Marinchio, R. Carminati, J. F. Torrado, G. Armelles, A. Garcia Martin, J. J. Saenz, *Opt. Express* **18** 3556-3567 (2010).
- [14] J. G. Kirkwood and J. Riseman, *J. Chem. Phys.* **16**, 565 (1948).
- [15] B. Carrasco and J. Garcia de la Torre, *J. Chem. Phys.* **111**, 4817 (1999).
- [16] B. Dahneke, *J. Aerosol Sci.* **1**, 179 (1982).
- [17] R. Millikan, *Phys. Rev.* **21**, 217 (1923).
- [18] J. Gieseler, L. Novotny and R. Quidant, *Nature Physics* **9**, 806 (2013); M. Yoneda and K. Aikawa, *J. Phys. B: At.Mol. Phys.* **50**, 245501 (2017).
- [19] J. Ahn, Z. Xu, J. Bang, Y. H. Deng, T. M. Hoang, Q. Han, R. M. Ma, and T. Li, *Phys. Rev. Lett.* **121**, 033603 (2018).
- [20] J. Corson, G. W. Mulholland, and M. R. Zachariah, *Phys. Rev. E* **96**, 013110 (2017)
- [21] M. Büttiker and R. Landauer *Phys. Rev. B* **30**, 1551 (1984).
- [22] H. Risken, Fokker-Planck equation, in *The Fokker-Planck Equation: Methods of Solution and Applications* (Springer, Berlin,1996).
- [23] Sivak D. A., Chodera J. D., Crooks G. E., *J. Phys. Chem. B*, **118**, 24, pp. 6466-6474 (2014)